Unveiling Morphology and Crystallinity Dynamics in $Ni_xMn_{1-x}CO_3$ Cathode Precursors through Batch Mode Co-precipitation

Jiajun Chen[a,c*], Arturo Gutierrez[a], Maksim A. Sultanov[b,e], Jianguo Wen[b], Jason R. Croy[a], Yan Wang[c], Venkat Srinivasan[d], and Pallab Barai[d]

[a]Chemical Sciences and Engineering Division, Argonne National Laboratory, Lemont, IL 60439, USA; [b]Center for Nanoscale Materials, Argonne National Laboratory, Lemont, IL 60439, USA; [c]Department of Mechanical & Materials Engineering, Worcester Polytechnic Institute, Worcester, MA 01609, USA; [d]Argonne National Laboratory, Lemont, IL 60439, USA; [e]Department of Physics, Northern Illinois University, Dekalb, IL 60115, USA

*email: jiajun.chen@anl.gov

Abstract

This study delves into the synthesis and control of $Ni_xMn_{1-x}CO_3$, a critical class of Mn-rich, Co-free precursors vital for cathode-oxide materials in energy storage and conversion technologies. Employing batch mode co-precipitation, we systematically generated samples with varying Ni concentrations (x=0, 0.1, 0.3, 0.5, 0.7, 0.9) and conducted a comprehensive analysis of their compositions, crystallinities, transition metal distributions, and particle morphologies through both experimental and computational methods. Significant variation in particle size and crystallinity was observed, contingent on Ni content. A pivotal transition emerged at Ni concentrations above x=~0.5, transforming uniform morphologies, such as spherical, monodisperse, pseudo single crystalline particles, into bimodal, polycrystalline structures. Furthermore, the study highlights the role of Ni-ammonia complexes leading to Ni-deficient precipitates and underscores the importance of ammonia concentration in achieving precise Ni content control. This study unveils critical reaction conditions governing Mn-rich precursor properties that are vital for cathode-oxides,

emphasizing the need for meticulous synthetic control and offering potential for practical applications in advanced energy storage and conversion systems.

Keywords

lithium-ion batteries, manganese-rich cathodes, particle morphology, nickel concentration, crystallinity, transition-metal distribution

1. Introduction

The development of lithium-ion batteries continues to be of great interest to the research community because of the ever-growing demand from the transportation sector.[1] In the past decade, the performance of Li-ion batteries has been improved greatly, due in large part to the development of cathode materials.[2] The current state of the art for lithium-ion battery cathodes are based in transition metal (TM) oxides, such as $LiNi_xMn_yCo_{1-x-y}O_2$ (NMC).[3] Additionally, potential next-generation cathodes are also largely based in TM oxide chemistries, such as Li-/Mn-rich oxides that are free of Co (LMR-NM), and the research community is regaining interest in these materials due to the potential economic benefits of using earth-abundant, Mn-rich chemistries. It has become increasingly clear that the processing method(s) used to synthesize a cathode material of choice play(s) a critical role in the resulting electrochemical performance, through modifying the resulting material characteristics, such as elemental homogeneity, phase purity, disorder/order ratio, and particle morphology.[4] Of specific interest here, it has been shown by experiment, theory, and electrochemical and techno-economic modeling, that the ultimate practicality of Li/Mn-rich cathodes is related to their synthesis-dependent properties across all length scales (e.g., atomic- to cell-level)[5, 6]. Therefore, it is necessary to more fundamentally understand the synthetic parameters

that allow greater control over desired characteristics of Mn-rich precursors themselves, which ultimately have significant influence over the final electrochemical performance.

The current state of the art, with respect to cathode precursor synthesis, is co-precipitation, which is carried out in a continuously stirred tank reactor under steady-state conditions (stated as CSTR from here forward). This method is capable of producing precursor particles with homogenous distributions of the TMs, uniform morphologies, and narrow size distributions.[7] Additionally, the microstructure of precursors produced via co-precipitation remain, typically, similar for the resultant TM oxide. Though co-precipitation is the most widely used route to produce divalent TM-hydroxides, $TM(OH)_2$, for cobalt and nickel-rich chemistries, there are some challenges when producing Mn-rich hydroxide precursors.[8-10] For example, the oxidation of Mn^{2+} occurs easily and forms impurities ($e.g.,\mathrm{MnOOH}$) in the precursor, leading to unwanted secondary phases, inhomogeneity, and structural distortions – all of which are undesirable with respect to subsequent lithiation/calcination of the final product. The control of the overall process to produce Mn-rich hydroxides is relatively complex because the material must be under an inert atmosphere to prevent the formation of these unwanted impurity phases. Consequently, Lee *et al.* introduced the carbonate co-precipitation method to synthesize cathode precursors for 5V spinel.[11] The divalent TM cations are relatively stable in the $TMCO_3$ precursors and prevent the formation of phase impurities; thus, carbonates have become the standard for the development of Mn-rich cathodes. Furthermore, in carbonate co-precipitation, the pH of the reaction is also relatively neutral (~7-9) compared with hydroxides (~10-12). Working at a lower pH can reduce equipment corrosion, mitigate safety risks from strongly alkaline solutions, and simplify waste disposal with decreased environmental impact.

Due to the effectiveness of CSTR co-precipitation to produce precursors for battery materials, many studies exist on understanding the reaction mechanisms/kinetics *and* on optimizing the parameters to control the morphology/properties of the precursor particles.[7, 12-14] The challenge of synthesizing ideal carbonate precursors under steady-state conditions is continual growth of secondary particle size, inhomogeneous metal distributions, and compositional deviations such as Ni deficiency when using ammonia as chelating agent.[7, 15] In addition, control over primary particle size and final secondary porosity has been shown to be difficult, but critical, for practical performance.[5] Moreover, during CSTR conditions there is a relatively large amount of waste produced. Compared with CSTR conditions(>24h), batch mode is more time efficient (<1h) and generates less amount of waste. Under batch mode, all reactants are mixed at the beginning, and the reaction is allowed to proceed without any further addition or removal of materials. The unique advantage of the batch mode is its simplicity; it can be operated even in a basic setup like a beaker, making it highly accessible and often used for smaller-scale preparations or experimental studies. Additionally, as opposed to the CSTR mode, using a batch mode allows the study to minimize the dynamics of the reaction.[16] Also, due to buffering effect of the of the ammonium bicarbonate, which is used in an excessive amount (ammonia over transition metal ratio is maintained at 15), helps to stabilize the pH of the reacting solution both before and after the precipitation of the transition metal carbonates. This choice simplifies computational modeling predictions and offers a clearer analysis of the process. Likewise, herein we choose a constant pH, consistent with previous reports [16], though pH certainly plays a crucial role.

There are existing studies using precursors produced by co-precipitation synthesis in batch mode.[11, 17-19] However, most of the existing studies using batch mode are generally focused on the electrochemistry of *one* target composition, and reports focused on the effects that synthesis

conditions have on morphological features are sparse. Nevertheless, some fundamental studies of Mn-rich carbonates produced using batch mode co-precipitation do exist. For example, the influence of solution chemistry on $MnCO_3$ particle morphology was investigated by *Robinson et al*. It was demonstrated that morphology and size of $MnCO_3$ can be tuned by moderate changes in reagent concentration, as the carbonate particles were shown to transform from rhombohedra to cubes to spheres by tuning the solution chemistry. They found that the $MnCO_3$ morphology is affected by the inoculation time and nucleation/growth of initial precipitates.[20] Additionally, *Garcia et al.* investigated the kinetics and dynamics of morphology evolution of $MnCO_3$ produced using batch mode co-precipitation. The evolution of rhombohedral shaped particles occurring under equilibrium conditions was revealed by computational analysis. It was determined that fast growth kinetics of the precipitates leads to a transition of the particle size and morphology (i.e., from rhombohedral to spherical).[16] These existing fundamental studies on $MnCO_3$ provide a strong foundation of understanding on how synthesis conditions greatly control the resulting morphologies. However, Mn only compositions are not extremely common for oxides used in Li-ion batteries compared with multicomponent Li-TM oxide materials, such as NMC and LMR-NM. Therefore, a need for fundamental understanding of multicomponent carbonates remains. Since the most recent trend has been to use little to no cobalt NMCs, due to high costs and geopolitical issues surrounding mining practices, the focus of the work herein is to understand the effects of introducing Ni into the synthesis of $Ni_xMn_{1-x}CO_3$ using a batch-mode reactor.

Understanding and controlling the morphology of particles produced through co-precipitation in batch mode is essential for comprehending the synthesis parameters that influence the particle morphology and characteristics. Crystallinity and the morphology/size of primaries are important parameters for cathodes and are known to influence electrochemical performance.[4, 21-25] A deep,

comprehensive and fundamental understanding of synthetic mechanisms and kinetics will be helpful for further optimization and better control of the processing and more effectively fine-tune methodologies, ensuring desired morphology and ultimately leading to enhancements in the final product's performance and consistency. In this study, the aim is to explore the co-precipitation processes employed in synthesizing the more complex, Ni-containing carbonate cathode precursors, focusing on the evolution of crystalline structures, TM distribution, and morphological attributes during synthesis as well as the impact on particle morphology of x in $Ni_xMn_{1-x}CO_3$. The precursor particles will be characterized in terms of surface area, elemental composition, particle size, morphology, and other relevant properties.

2. Methodology

2.1 Synthesis of precursors

Carbonate precursors in this study were prepared via batch mode co-precipitation involving two starting solutions. Solution A: 1200mL of $MnSO_4 \cdot H2O$ and $NiSO_4 \cdot 6H2O$ dissolved in DI water at target concentrations. Solution B: 1200mL of NH_4HCO_3 (Fisher) dissolved in DI water at target concentrations. The two solutions were preheated to a temperature of 50℃. Subsequently, solution B was poured into solution A and the mixture was stirred with a magnetic stirrer for 1 hour at 500rpm. The precursor powder was rinsed with DI water and ethanol then filtered, followed by overnight drying (~15 hours) in an oven purged with nitrogen at 110 °C.

2.2 Characterization of precursor

The crystal structure and morphology of the co-precipitated precursor particles were examined by X-ray Diffraction (XRD, Rigaku by SmartLab) and Scanning Electron Microscopy (SEM, JEOL NeoScope JCM-6000Plus). The particle size was examined by a Particle Size Analyzer (PSA,

CILAS 1090) and the surface area of the particles was tested by an automated gas sorption analyzer (BET, Autosorb iQ). The chemical compositions of the samples were determined using Inductively Coupled Plasma Mass Spectrometry (ICP-MS) conducted on an Agilent instrument. The analysis was performed according to standard protocols to ensure accuracy and reliability of the results.

Further analysis such as EDS data acquisition, HRTEM imaging and SAED pattern acquisition was conducted using the FEI Talos F200X TEM/STEM at an accelerating voltage of 200 kV. Powder samples for TEM analysis were adhered to a protective Al film placed over a 3 mm Cu TEM grid with a 2 mm circular aperture, followed by a low-angle ion milling process. Commercial software DigitalMicrograph by Gatan was then used to analyze the diffraction patterns and the FFT of high-resolution images in order to better understand the crystallinity of the study materials, as well as the primary particle size analysis.

2.3 Electrochemical characterization

A NiMn carbonate precursor was mixed with the desired amount of lithium carbonate (Li_2CO_3) and fired at 850 ℃ for 20 h in air. The cathode-electrode was prepared with a slurry consisting of a ratio of 84:8:8 active material: Super P carbon: polyvinylidene fluoride (PVDF) coated on aluminum foil. The slurry was cast to achieve an active loading of ~8 mg/cm^2. The cathode was cycled in 2032-type coin cells against lithium metal with Celgard 2030 separators. All tests were conducted in a temperature-controlled oven held at 30℃.

2.4 Computational modeling

Table 1. List of chemical reactions, and corresponding equilibrium constants, used to solve the species balance relations shown in Eq. (1) – (5).

List of chemical reactions	Equilibrium constants (K_{eq})
$NH_4^+ + OH^- \rightleftharpoons NH_4OH$	6.3095×10^4
$H^+ + CO_3^{2-} \rightleftharpoons HCO_3^-$	1.7793×10^{10}
$H^+ + HCO_3^- \rightleftharpoons H_2CO_3$	2.3255×10^6
$Ni^{2+} + NH_3 \rightleftharpoons [Ni(NH_3)]^{2+}$	6.4565×10^2
$Ni^{2+} + 2NH_3 \rightleftharpoons [Ni(NH_3)_2]^{2+}$	1.2022×10^5
$Ni^{2+} + 3NH_3 \rightleftharpoons [Ni(NH_3)_3]^{2+}$	7.0794×10^6
$Ni^{2+} + 4NH_3 \rightleftharpoons [Ni(NH_3)_4]^{2+}$	1.3182×10^8
$Ni^{2+} + 5NH_3 \rightleftharpoons [Ni(NH_3)_5]^{2+}$	8.5113×10^8
$Ni^{2+} + 6NH_3 \rightleftharpoons [Ni(NH_3)_6]^{2+}$	1.2022×10^9
$Mn^{2+} + NH_3 \rightleftharpoons [Mn(NH_3)]^{2+}$	10^1
$Mn^{2+} + 2NH_3 \rightleftharpoons [Mn(NH_3)_2]^{2+}$	3.4673×10^1
$Mn^{2+} + 3NH_3 \rightleftharpoons [Mn(NH_3)_3]^{2+}$	5.0118×10^1
$Mn^{2+} + 4NH_3 \rightleftharpoons [Mn(NH_3)_4]^{2+}$	1.9952×10^1

From the total amount of $TMSO_4$ (specifically mixture of $NiSO_4$ and $MnSO_4$) and NH_4HCO_3 added to the solution, the concentration of free transition metal cations (Ni^{2+} and Mn^{2+}) and carbonate anions (CO_3^{2-}) within the solution is estimated by solving the mass balance equations 1-5 below. The mass balance of individual species considers the equilibrium relations and the corresponding chemical equilibrium constants. Concentration of H^+ cations and OH^- anions, in

other words pH of the solution, is also estimated from the charge neutrality and the constant magnitude of the product of the ionic concentration of H^+ and OH^- ions.[10, 15]

$$\bar{c}_{Ni^{2+}} = [Ni^{2+}] + [Ni(NH_3)]^{2+} + [Ni(NH_3)_2]^{2+} + [Ni(NH_3)_3]^{2+} + [Ni(NH_3)_4]^{2+} + [Ni(NH_3)_5]^{2+} + [Ni(NH_3)_6]^{2+} \quad (1)$$

$$\bar{c}_{Mn^{2+}} = [Mn^{2+}] + [Mn(NH_3)]^{2+} + [Mn(NH_3)_2]^{2+} + [Mn(NH_3)_3]^{2+} + [Mn(NH_3)_4]^{2+} \quad (2)$$

$$\bar{c}_{CO_3^-} = [HCO_3^-] + [H_2CO_3] + [CO_3^{2-}] \quad (3)$$

$$\bar{c}_{NH_3} = [NH_3] + [NH_4^+] + [Ni(NH_3)]^{2+} + 2[Ni(NH_3)_2]^{2+} + 3[Ni(NH_3)_3]^{2+} + 4[Ni(NH_3)_4]^{2+} + 5[Ni(NH_3)_5]^{2+} + 6[Ni(NH_3)_6]^{2+} + [Mn(NH_3)]^{2+} + 2[Mn(NH_3)_2]^{2+} + 3[Mn(NH_3)_3]^{2+} + 4[Mn(NH_3)_4]^{2+} \quad (4)$$

$$[H^+] \cdot [OH^-] = 10^{-14} \quad (5)$$

$$2([Ni^{2+}] + [Ni(NH_3)]^{2+} + [Ni(NH_3)_2]^{2+} + [Ni(NH_3)_3]^{2+} + [Ni(NH_3)_4]^{2+} + [Ni(NH_3)_5]^{2+} + [Ni(NH_3)_6]^{2+}) + 2([Mn^{2+}] + [Mn(NH_3)]^{2+} + [Mn(NH_3)_2]^{2+} + [Mn(NH_3)_3]^{2+} + [Mn(NH_3)_4]^{2+}) + [NH_4^+] + [H^+] - [HCO_3^-] - 2[CO_3^{2-}] - [OH^-] - 2[SO_4^{2-}] = 0 \quad (6)$$

Here, $\bar{c}_{Ni^{2+}}$, $\bar{c}_{Mn^{2+}}$, and $\bar{c}_{CO_3^-}$ are the concentrations of Ni^{2+}, Mn^{2+}, and CO_3^- that are present within the solution, which is estimated by subtracting the amount of nickel and manganese that gets removed from the solution due to precipitation in the form of $NiCO_3$, $MnCO_3$, $Ni(OH)_2$, and $Mn(OH)_2$. $\bar{c}_{NH_3}$ is the concentration of ammonia that is initially added to the solution, and it is assumed that no ammonia is removed from the solution in the form of gas. All the other expressions inside the brackets ($[\cdot]$) indicate concentration of that particular species in mol/L units. The chemical reactions and the corresponding equilibrium constants (Table 1) are also taken into consideration while solving for the species balance relations.

Under supersaturated conditions, precipitation of the individual species leads to the formation of the primary and secondary particles. Formation of these particles involves two steps:[16, 26]

1. Nucleation, where small nuclei of the individual precipitates form within the solution of the supersaturated reactants through a homogeneous nucleation mechanism.
2. Growth, where the formed nuclei grow in size due to further precipitation through the direct, or surface growth, mechanism.

For maintaining simplicity of the developed computational model, the nucleation and growth of only the secondary particles are simulated. Also, a spherical shape of the secondary particles is considered in this developed model. Both nucleation and growth of the particles depend strongly on the supersaturation ratio (SSR) of the precipitating compound within the reacting solution, which is defined as:

$$\mathrm{SSR} = [\mathrm{TM}^{2+}] \cdot [\mathrm{CO}_3^{2-}] / K_{\mathrm{SP,TMCO_3}} \tag{7}$$

Here, $[\mathrm{TM}^{2+}]$ indicates the concentration of either Ni^{2+} or Mn^{2+} and $K_{\mathrm{SP,TMCO_3}}$ indicates the solubility product of that particular $\mathrm{TMCO_3}$ being precipitated. Precipitation of $\mathrm{TM(OH)_2}$ is also taken into account, but the overall precipitation of hydroxides is negligible due to the relatively low pH (pH < 8.5) being maintained during the precipitation reactions. All the solubility products for the $\mathrm{TMCO_3}$ and the $\mathrm{TM(OH)_2}$ being taken into consideration for estimation of the magnitude of SSR are provided in Table 2.

Table 2. List of precipitation reactions, and corresponding solubility products, used to estimate the amount of precipitate and growth of precipitated particles

List of precipitation reactions	Solubility products (K_{sp})
$\mathrm{Ni^{2+} + 2OH^- \rightleftharpoons Ni(OH)_2}$	6.0266×10^{-16}
$\mathrm{Mn^{2+} + 2OH^- \rightleftharpoons Mn(OH)_2}$	1.9953×10^{-13}
$\mathrm{Ni^{2+} + CO_3^{2-} \rightleftharpoons NiCO_3}$	1.42×10^{-7}
$\mathrm{Mn^{2+} + CO_3^{2-} \rightleftharpoons MnCO_3}$	2.34×10^{-11}

To capture the nucleation density of the particles, a classical nucleation theory-based computational methodology is adopted (for more details please check an earlier publication by some of the co-authors, Barai et al., *Journal of Physical Chemistry B* (2019) 3291).[26] Growth of each secondary particle is modeled as a reaction precipitation process. Rate of increase in particle size is simulated as:

$$\frac{dr_{\mathrm{sp}}}{dt} = k_{\mathrm{reac}} \cdot c_{\mathrm{eq,TMCO_3}} \cdot (\mathrm{SSR} - 1) \tag{8}$$

where, r_{sp} indicates the radius of the secondary particles, t denotes time, k_{reac} is the reaction rate constant that can be a function of temperature (T), $c_{\mathrm{eq,TMCO_3}}$ is the equilibrium concentration of the $\mathrm{TMCO_3}$ within the solution, which is defined as the square root of the solubility product $\left(c_{\mathrm{eq,TMCO_3}} = \sqrt{K_{\mathrm{SP,TMCO_3}}}\right)$. The dependance of the reaction rate constant on the local temperature is captured through an Arrhenius-type relation:

$$k_{\mathrm{reac}} = k_{\mathrm{reac,0}} \cdot \exp\left(\frac{-E_{\mathrm{a}}}{RT}\right) \tag{9}$$

where, $k_{\mathrm{reac,0}}$ is the reference reaction coefficient (Table S1), E_{a} is the activation energy (Table S1), and R denotes the universal gas constant. Note that the direct growth of the secondary

particles is simulated here, which is assumed to occur either through a direct precipitation, or a surface nucleation (and surface growth), or a combination of the two. The computational model does not differentiate between the details of the growth mechanism, but rather tries to simulate it as a precipitation-induced growth process. Note that even though all the reactants are added instantaneously, at the beginning of the reaction, all the nucleation of secondary particles does not occur at the initial timestep. Rather, nucleation proceeds with time, while the largest nucleation density is observed right after mixing all the reactants, which eventually decreases with time because of the decrease in SSR. Since different particles nucleate at different timesteps, they demonstrate different sizes at the end of the reaction. The average particle size is estimated by conducting a volume averaging over all the particles. The parameters involved in simulating the particle growth process are provided in Table S1 (see supplemental materials).

3.Results and discussion

In this study, the co-precipitation of $Ni_xMn_{1-x}CO_3$ was carried out in a batch reactor. We explored the morphology and chemical composition of the resultant particles through experimental analysis and computational modeling. The following aspects will be discussed:

i) The precipitation of $Ni_xMn_{1-x}CO_3$, including the primary particle size and crystallinity of the precipitates.
ii) The size and morphology of the secondary particles and the model predictions.
iii) The composition and distribution of the transition metals within the precipitates and the underlying reaction mechanism.
iv) The electrochemistry of lithiated LMR-NM cathode with $Ni_xMn_{1-x}CO_3$ (x=0.35) precursor.

3.1 Crystallinity of the precipitates

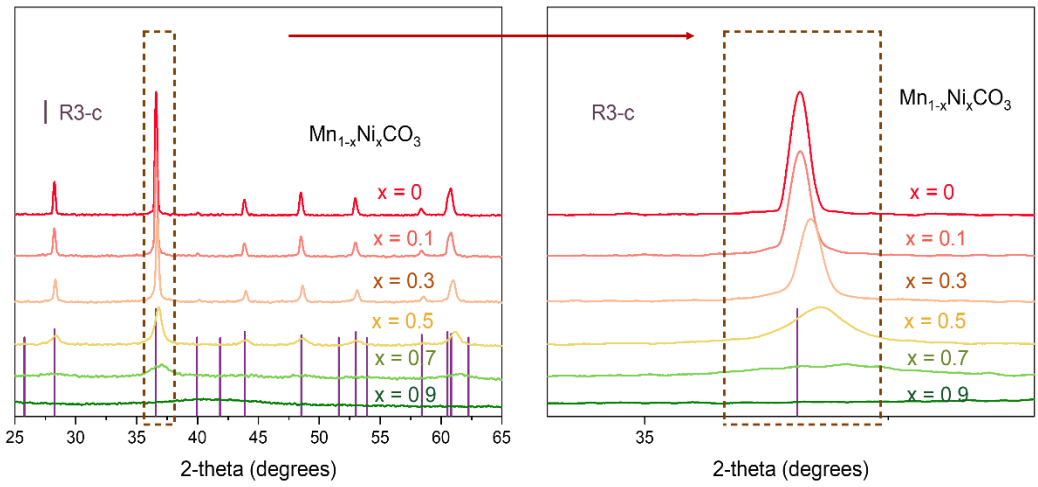

Figure 1. X-ray diffraction data of samples $Ni_xMn_{1-x}CO_3$, x=0 to x=0.9 (from top to bottom), purple drop line indexed to R-3c phase

The effect of increasing the Ni content in the carbonate precursor was investigated through batch mode synthesis of a series of samples $Ni_xMn_{1-x}CO_3$ (x=0, 0.1, 0.3, 0.5, 0.7, 0.9). All other conditions were kept constant (metal concentration = 12mM, $[NH_4^+]/[TM^{2+}]$ = 15:1, reaction temperature: 50℃, stirring speed: 500rpm). The XRD patterns of all samples were compared to the expected calcite phase (w/ space group R-3c), as shown in Figure 1. The samples with lower Ni contents from x=0 to x=0.5 are easily indexed to the expected calcite phase, as all main peaks are discernible. As the amount of targeted Ni increased, the peaks appeared to broaden noticeably at x = 0.5, as manifested clearly in the main peak enclosed by the dashed red box in Figure 1. The peak broadening suggests that increasing the Ni content may be playing a role in the crystallite size and perhaps strain of the resulting structure of the $Ni_xMn_{1-x}CO_3$ powders. At even higher concentrations of Ni (x=0.7 and 0.9), the samples appear to be amorphous, though two broad peaks are still visible near expected 2-theta for x=0.7.

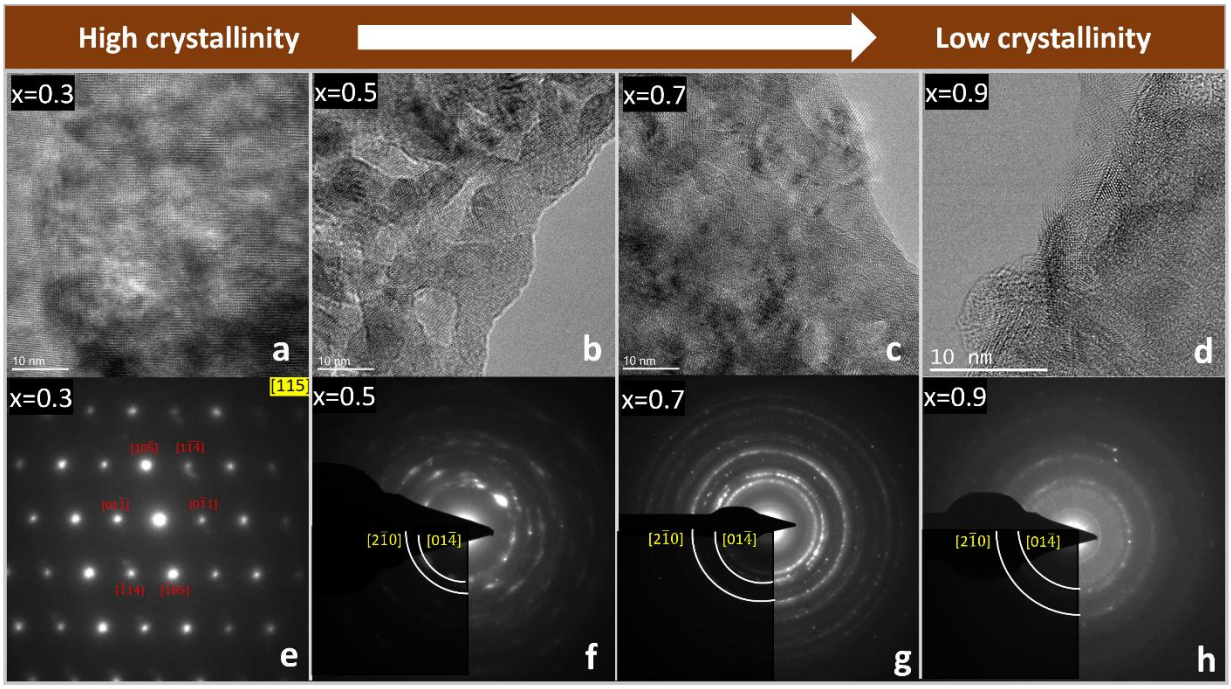

Figure 2. HRTEM (a-d) and SAED (e-h) of $Ni_xMn_{1-x}CO_3$, x=0.3, x=0.5, x=0.7, x=0.9

Because phase identification was ambiguous for x=0.7 and 0.9 using XRD, further analysis via TEM was performed. Figure 2 shows HRTEM(a-d) and selected area electron diffraction (SAED) (e-h) carried out on the x= 0.3, 0.5, 0.7, and 0.9 powders. Upon initial inspection (Figure 2 a-d), each sample demonstrates a clearly discernable atomic lattice, including x=0.7 and 0.9, thus confirming the crystallinity of the samples. Further inspection of the SAED (Figure 2 e-h) and the simulation-based analysis conducted using jems software package developed by Dr. Pierre Stadelmann[27] confirms all samples formed into the calcite structure but with clear differences in crystallinity. Notable is the presence of pseudo monocrystalline domains in the x=0.5 sample, which was further investigated and confirmed to be present in the other samples (Supplementary Figure S1).Previous work on $MnCO_3$ resulted in the precipitation of *pseudo* single crystal particles at similar metal concentration as used here (12mM), as well as lower concentrations.[16] A pseudo single crystal can have grain boundaries within the particle while single crystals do not. Furthermore, a pseudo single crystal has no internal porosity, which differentiates them from

conventional secondary particles. In this work, pseudo single crystal particles precipitated at lower Ni contents but a transition to polycrystalline particles occurred at higher levels of Ni. For example, the SAED for the x=0.3 sample exhibits a regular array of spots in the diffraction pattern, characteristic of single crystal particles. On the other hand, concentric rings begin to manifest in the diffraction pattern of the x=0.5 sample and become more obvious in x = 0.7 and 0.9 samples. The presence of the concentric ring for x=0.5 to 0.9 samples reveals a transition from single crystal at low Ni concentrations ($x \leq 0.3$) to polycrystalline particles at higher concentrations of Ni. Indeed, using IFFT (Inverse Fast Fourier Transition) analysis, the approximate grain size was obtained from the HRTEM images. The grain size was found to decrease with increasing Ni content from 100nm for x=0.3, 40nm for x=0.5, to 10nm for x=0.9. The transition from single crystal to polycrystalline particles at x = 0.5, as determined from the SAED and IFFT analysis, suggests the observed broadening of XRD peaks mentioned above is largely due to decreasing grain size with increasing Ni content. The model predicted size of the primary particles as a function of Ni content is shown in Figure 5 as a function of the Ni content by the black solid line. Experimentally observed primary particle sizes/grain size are denoted by the black squares, which correlates well with the model predictions. In order to decipher the decrease in primary particle size, a computational methodology is developed using the lattice-based Monte Carlo technique that can capture the competition between the "rate of nucleation" and "rate of growth" experienced by the primary particles. Since growth of the secondary particles occur through nucleation on existing surface, this can be characterized as heterogeneous nucleation. Unlike homogeneous nucleation, heterogeneous nucleation mechanism does not depend strongly on the supersaturation ratio. As long as the supersaturation ratio is greater than unity (SSR > 1), heterogeneous nucleation can occur given sufficient sites are available. Accordingly, the rate of heterogeneous nucleation

depends on the availability of sites on the surface of the existing particles where the heterogeneous nucleation can occur. (see equations S1-S4 in supplemental materials). Surface nucleation usually tends to occur on pre-existing defects. Due to the crystalline nature of the $MnCO_3$ precipitates, the number of sites for surface nucleation are relatively less, which leads to smaller magnitudes of nucleation rate constants. However, $NiCO_3$ demonstrates an amorphous-like crystal structure, which leads to substantially larger amount of surface nucleation sites, and eventually very large surface nucleation rate constants $\left(k_{\mathrm{sn,NiCO_3}} > k_{\mathrm{sn,MnCO_3}}\right)$. Accordingly, with increasing Ni-content, the "reaction rate constant" for growth of primary particles decreases, and their propensity for "surface nucleation" increases. As a result, Mn-rich precipitates end up with larger primary particles and smaller number of surface nuclei, whereas Ni-rich precipitates demonstrate smaller primaries and larger amount of surface nuclei.

3.2 Morphology of the particle

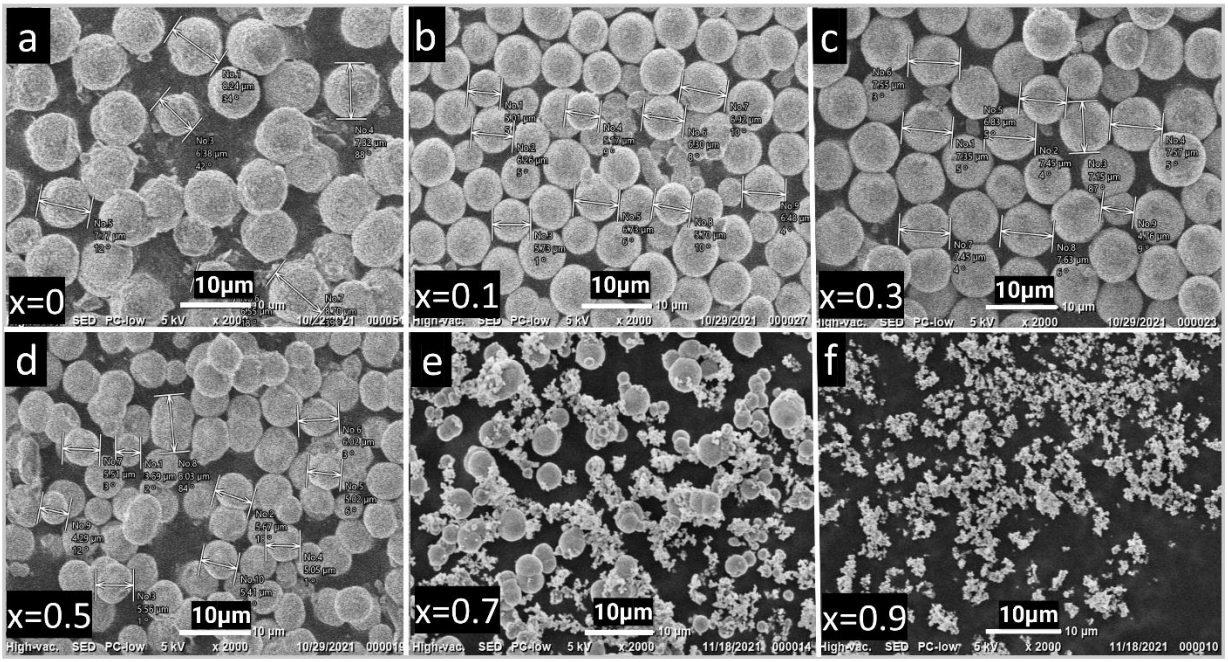

Figure 3. Physical characterization of precursors synthesized under batch mode reaction with varying Ni content: (a-f) SEM images of precursors $Ni_xMn_{1-x}CO_3$ of (a)x=0 (b) x=0.1, (c) x= 0.3, (d) x= 0.5, (e) x= 0.7, (f) x= 0.9

Secondary particle morphology: The particle size of the $Ni_xMn_{1-x}CO_3$ samples was visually inspected by SEM as shown in Figure 3 (a-f). No obvious trend or variation of secondary particle size and shape was observed for samples from x=0 to x=0.5. All secondary particles were spherical and had an average diameter of 8-10 microns. For precipitation of work on $MnCO_3$ (i.e. x = 0), our earlier work[16] achieved much smaller secondary particles. The difference in particle size between previous work and the current work is likely due to the different HCO_3^- to TM^{2+} ratios used, dictated here by the initial NH_4HCO_3 solution. 15:1 herein compared to (40:1) in the previous report. The amount of CO_3^{2-} in solution used in this work results in a different SSR, which results in a different nucleation density that ultimately leads to variations in formation and growth of secondary particles. However, the work of *Robinson et al* used various amounts of HCO_3^-: TM^{2+} ratios, and their analysis resulted in particle sizes similar to the particle sizes what was observed

in this work for the x=0 sample ($MnCO_3$).[20] As the intended amount of Ni content increased to x=0.7 (Figure 3e), an additional set of much smaller particles (submicron) precipitated along with the larger spherical particles. When the Ni content was increased even further to x=0.9 (Figure 3f), only smaller particles (submicron) were observed in the final product. The precipitation of the smaller particles, which began at x=0.7, suggests competing nucleation events are at play in this range of Ni content ($0.5 < x \leq 0.7$) leading to the two particle sizes, while outside of this range ($x \leq \sim 0.5$) there is only one dominant pathway leading to a single particle size distribution. This will be discussed further below.

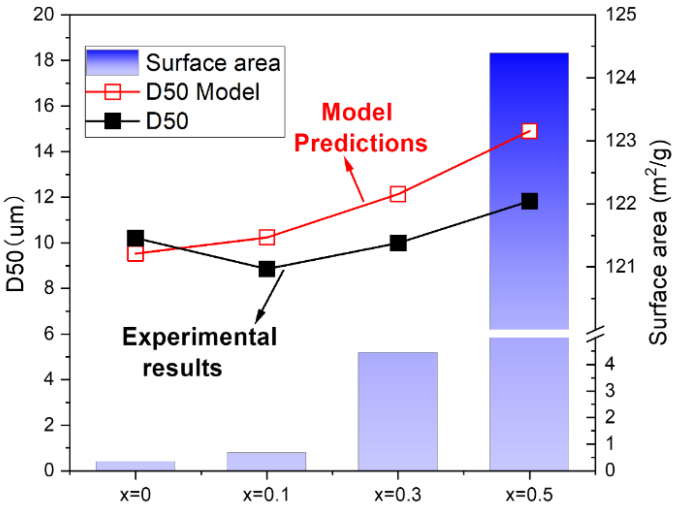

Figure 4. Physical characterization results of precursors synthesized under batch mode reactions with varying Ni contents, x (x axis), surface areas (right axis, note the break above $4m^2/g$), and particle sizes.

The particle size analysis (PSA) of the x=0 to x=0.5 samples is shown in Figure 4. Though the size differences are not significant between the samples, a comparison to the computationally predicted size may reveal insights into the mechanisms and driving forces of growth. The average particle size decreases from x=0 to x=0.1, then systematically increases as x increases from 0.1 to 0.5. Before discussing the computational results, it should be reiterated that the concentration of metals ($[Mn^{2+}] + [Ni^{2+}]$) for each reaction was constant. Based on the modeling predictions, during the

precipitation of $Ni_xMn_{1-x}CO_3$ precursors, $MnCO_3$ is expected to form the initial nuclei because of its lower solubility product (than $NiCO_3$) and higher supersaturation ratio in this range of x. The supersaturation ratios for $NiCO_3$ and $MnCO_3$ is estimated from the concentration of free ions for all the different fractions of Ni, which is plotted in Figure S3. It is evident that due to the smaller solubility product of $MnCO_3$ than $NiCO_3$, the supersaturation ratio of the $MnCO_3$ is substantially larger than that of the $NiCO_3$. Also, note that the formation of the Ni-ammonia complex contributes to a decrease in free Ni^{2+} cations in the reaction solution, which further lowers the supersaturation ratio of $NiCO_3$. Growth of these nuclei occurs through precipitation of $TMCO_3$ from the solution either through direct precipitation, or through the surface nucleation and surface growth mechanism. While maintaining a constant concentration of TMs overall, an increase in the amount of Ni^{2+} in the solution leads to a decrease in the concentration of Mn^{2+}. Consequently, this causes a reduction in the supersaturation ratio of $MnCO_3$, which reduces the number of nuclei as the concentration of Ni in the solution increases. A decrease in nucleation density leads to the formation of larger secondary particles because each nucleus has more available metals in solution after the initial nucleation event. The model predicts an increase in particle size with a higher concentration of Ni^{2+} cations in the solution. Nevertheless, the computational model used is unable to capture the two types of precipitates observed beyond x = 0.5, therefore, the comparison was limited to $Ni_xMn_{1-x}CO_3$, x = 0.0-0.5.

The experimentally observed secondary particle size of the x=0, $MnCO_3$ dropped slightly before increasing with the Ni concentration, as shown in Figure 4. However, the computational model is unable to capture this nuance. The present simulations assume similar reaction rate constants for both $MnCO_3$ and $NiCO_3$. The larger size of the $MnCO_3$ precipitates can possibly be attributed to the faster reaction rate constant associated with the precipitation of $MnCO_3$. If it is hypothesized

that coprecipitation of $Ni_xMn_{1-x}CO_3$ slows down the reaction rate constant, then the decrease in particle size can be captured successfully. The reason for Ni slowing down the precipitation of $Ni_xMn_{1-x}CO_3$ can be attributed to the fact that when both Ni and Mn precipitate together, the driving force for Ni to get out of the solution is much less than the driving force for Mn to get out (due to the difference in supersaturation ratio). This can lead to the variation in reaction rate constants.

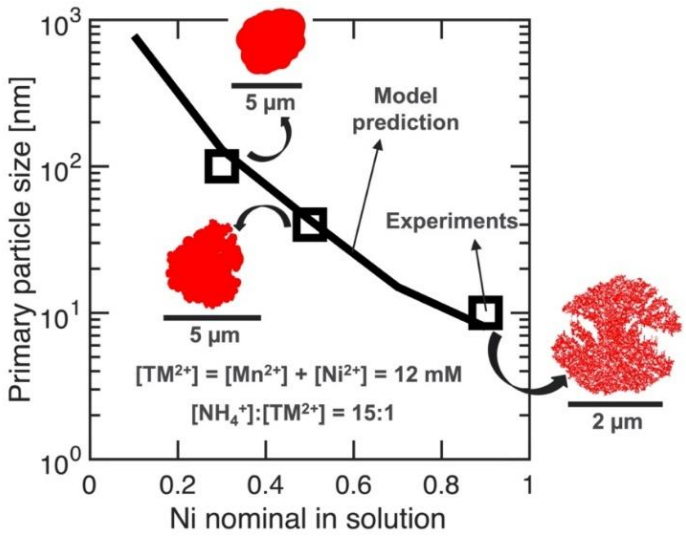

Figure 5. Comparison between model predicted (black solid line) and experimentally observed (black squares) primary particle sizes as a function of fractional Ni content within the reacting solution. The model predicted distribution of primary particles within the secondary particle is also denoted by the inset images in red.

Modeling of particle morphology: It is observed in SAED (Figure 2 e-h) that as the amount of Ni^{2+} cations are altered, the primary particle morphology of the precipitate changes significantly. For larger amount of Mn, pseudo-single-crystalline precipitates are observed with larger primary particles. As the fraction of Ni within the solution increases, the precipitate starts to look more polycrystalline with smaller primary particle size. Also, porosities start to evolve within the precipitates with increasing amount of Ni cations. The surface area of the x = 0.0 – 0.5 samples were also compared. This subset of samples was chosen for comparison because the average particle size did not change drastically for x=0-0.5, as noted above. On the other hand, the average

particle size decreased significantly from ~10-micron particles to much smaller, submicron particles as the Ni content increased beyond x = 0.5, which would affect the measured surface area. The measured surface area did increase as the Ni content increased from x = 0.0 – 0.5, as shown in Figure 4. To capture the trend of surface area, the computationally predicted secondary particle morphologies are shown, as inset images of Figure 5, in red for Ni fractions of x = 0.3, 0.5 and 0.9. These secondary particles form through the "surface nucleation" induced growth process. Particles with larger Ni content experience very high "surface nucleation densities", where diffusion of transition metal within the reacting solution becomes the limiting factor, which leads to non-uniform surface nucleation process. This non-uniformities in precipitation leads to the formation of porous microstructures in Ni rich samples. On the contrary, decreasing the Ni content results in smaller "rates of surface nucleation" and the surface nuclei form in a fashion that minimizes surface area without the formation of any pores, and eventually surface energy of the precipitates are minimized. The parameters used for running the simulations are provided in Table S2.

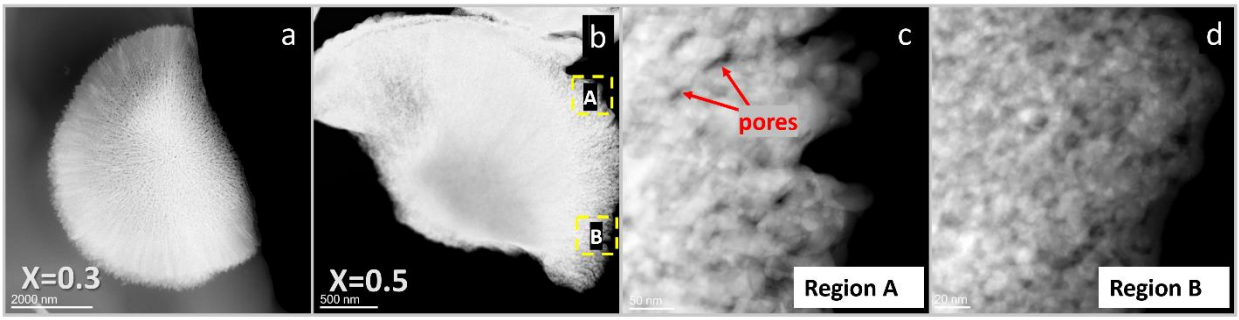

Figure 6. HAADF images of Internal porosity of $Ni_xMn_{1-x}CO_3$, (a)x= 0.3, (b), (c), (d): x= 0.5, the dark domains in the image are the pores

The increase in surface area appears exponential in nature, as the increase was relatively subtle for x=0-0.3 (e.g., x=0: 0.337m^2/g; x=0.1: 0.672m^2/g; x=0.3: 4.439m^2/g) compared to the dramatic increase that occurred between x=0.3 and x=0.5 (4.439m^2/g to 124.393m^2/g: note the break in y-axis). Representative HAADF images of particles for the x=0.3 and x=0.5 samples are shown in

Figure 6. There are obvious nanosized pores in both samples, but the location of the pores may provide some explanation for the drastic difference in the measured BET values between these two samples. Further inspection of the x=0.3 sample reveals a denser outer shell with a more porous core, while the x=0.5 sample shows a feather-like, porous surface. When measuring the surface areas by BET, the internal pores in the core of the x=0.3 sample are not measured because of the dense outer shell, while the porous surface of the x=0.5 is fully accessible. Model predicted surface porosities simulated by Lattice based Monte Carlo is also plotted in Figure S4. For x = 0.3 sample, the absence of empty lattice sites on the surface results in no surface porosity. Conversely, the x = 0.5 sample has numerous empty lattice sites, resulting in increased porosity in the secondary particle.

3.3 Transition metal composition and distribution within the precipitates

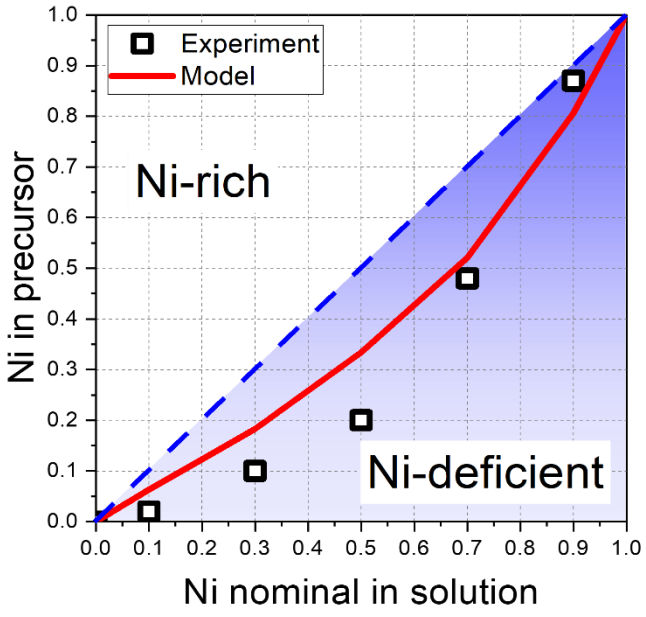

Figure 7. Physical characterization of precursors synthesized under batch mode reactions with varying Ni contents: ICP-MS analysis results of precursors and Model predictions of precipitates. The Black squares are the experimental measurements and the red line represents modeling predictions. The blue dashed line represents the targeted value of Ni content in the product. The shaded blue region, below the blue line, represents a region where the Ni content in the final product is less than the target value (Ni deficient). The white region represents a region where the Ni content in the final product is higher than the target value (Ni-rich).

Figure 7 shows the concentration of Ni in the final product as a function of the intended Ni amount. The blue dashed line represents the targeted Ni concentration for each of the samples. The shaded blue region, below the blue line, represents a region where the final product is Ni deficient. Experimental results from ICP-MS analysis (black squares) revealed most of the samples are Ni deficient, with the exception of the extremes at x= 0 and 0.9 (x=0.1: $Ni_{0.02}Mn_{0.98}CO_3$; x=0.3: $Ni_{0.1}Mn_{0.9}CO_3$; x=0.5: $Ni_{0.2}Mn_{0.8}CO_3$; x=0.7: $Ni_{0.48}Mn_{0.52}CO_3$; x=0.9: $Ni_{0.87}Mn_{0.13}CO_3$). The experimental conditions of the reactions were used to predict the amount of Ni in the final product using computational analysis and the results are also plotted in Figure 7 (red line). As can be seen from the figure, the predicted composition of the samples fits the experimental results. The Ni deficiency observed in the majority of the samples (x = 0.1-0.7) has two potentially contributing factors. First, $NiCO_3$ is a more soluble substance when compared to $MnCO_3$ as evidenced by the higher solubility product (K_{sp}) for $NiCO_3$ when compared to $MnCO_3$ (see Table 2 for the exact numbers). The higher K_{sp} results in a smaller supersaturation ratio for $NiCO_3$ leading to less overall precipitation. The second contributing factor leading to Ni deficiency is related to the formation of the nickel-ammonia complex (denoted as $[Ni(NH_3)_n]^{2+}$). The formation of this complex tends to further increase the solubility of Ni^{2+} cations within the solution, and effectively lowers the precipitation of $NiCO_3$ even further. These two factors, in a combined fashion, lead to a lower amount of precipitated $NiCO_3$, which is reflected in the formation of nickel deficient carbonate precipitates for x = 0.1-0.7, as shown in Figure 7. Making Ni the major constituent in the solution ($x = 0.9$) leads to the formation of a carbonate nearly matching the intended Ni amount.[26].

3.4 Validation of Modelling Results and Loss of Ni

In order to test the modelling results and mitigate the loss of Ni associated with ammonia, as described above, an additional reaction was carried out using sodium bicarbonate ($NaHCO_3$) to

replace ammonia bicarbonate as the source of CO_3^{2-} anions. The targeted composition was $Ni_{0.35}Mn_{0.65}CO_3$ (x=0.35), where Ni deficiency was predicted and observed to be relatively high when using ammonia bicarbonate. ICP-MS analysis revealed the sample prepared with sodium bicarbonate was not Ni deficient, resulting in a composition of $Ni_{0.34}Mn_{0.66}CO_3$, very close to the targeted value of x=0.35. The computational model also predicted almost complete precipitation of the Ni cations from the reacting solution in the absence of ammonia. This result provides strong evidence that the formation of nickel-ammonia complex plays the major role in the observed Ni deficiency when using ammonia bicarbonate as the source of CO_3^{2-} anions.[28-30]

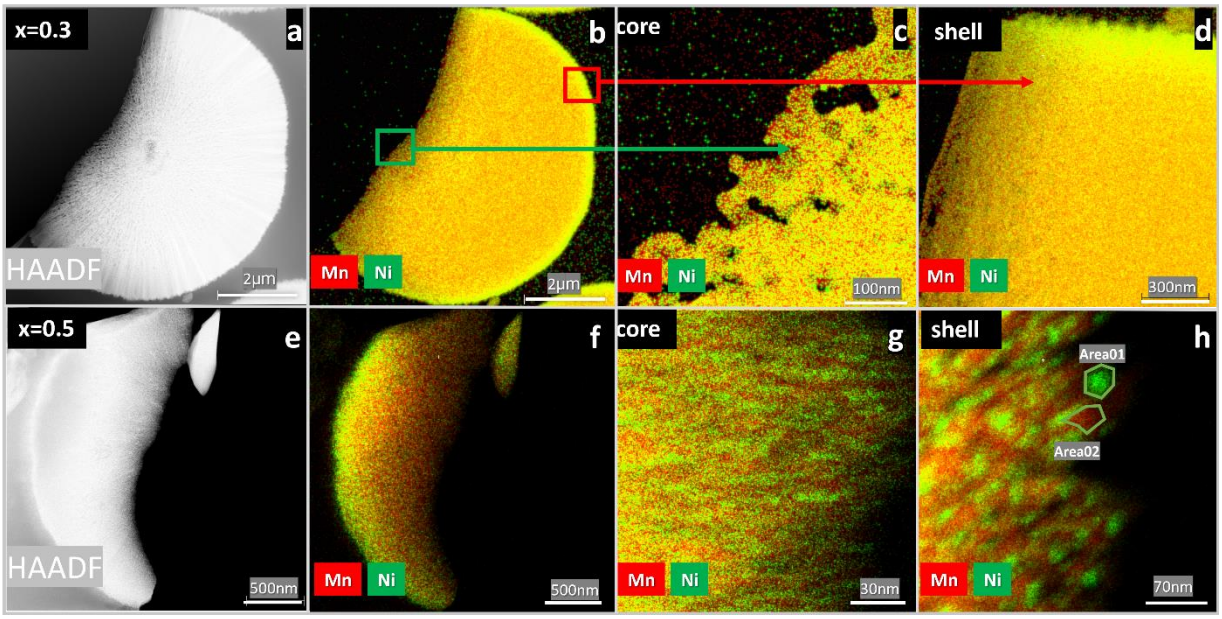

Figure 8. STEM-EDS mapping of transition metals of $Ni_xMn_{1-x}CO_3$ x=0.3(a-d), x=0.5(e-h)

In terms of the TM distribution within the particles, the x=0.3 and x=0.5 samples were studied by STEM-EDS as shown in Figure 8. The distribution of TMs in the bulk of the particles was found to be uniform, but a higher concentration of Ni was observed at the surface of the particles, which resulted in core-shell-like particles. For example, the STEM-EDS mapping of Mn and Ni for x=0.3,

Figure 8 (a-d), clearly illustrates a thin shell at the surface with an increased amount of Ni (17.82% of Ni) compared to the core region (7.53% of Ni). Furthermore, STEM-EDS mapping of Mn and Ni for x=0.5, Figure 8 (e-h), also reveals the presence of a core-shell structure with regions near the surface exhibiting a higher concentration of Ni (19.98% of Ni) compared to the bulk (13.46% of Ni). The enrichment of Ni on the surface of the secondary particles resulted in nanometer-sized regions with significantly different concentrations of Ni, as shown in Figure 8(h). For example, a region of ~35 nm in diameter (labeled Area 01, 8(h)) is found to contain 56.67% of Ni, while Area 02 contains 12.41% of Ni. The growing heterogeneity of the surface as the Ni content increased from x = 0.3 to 0.5, along with the two drastically different particle sizes observed for x = 0.7 (Figure 3e), suggests Ni and Mn prefer unique reaction pathways. The reaction rate constant for precipitation decreases with increasing Ni content. As a result, Mn rich samples grow by direct precipitation, whereas, Ni rich samples prefer to grow by surface nucleation and surface growth phenomena. Indeed, STEM-EDS mapping for x = 0.7 (Figure S2) revealed that the smaller sub-micron particles have higher Ni content (69.80%, which is near the target Ni concentration) and the larger particles (average size of 2-3 microns) had lower Ni content (44.57%).

The Ni enrichment observed at the surface of the x = 0.3 and 0.5 particles might be hypothesized, again, to be associated with the lower solubility product of $MnCO_3$. As already discussed above, since the precipitation of $MnCO_3$ is favored when compared to $NiCO_3$, the available Mn initially precipitates faster, along with the lower proportion of available Ni in solution, to form the center of the particles. As the reaction progresses, with a more rapidly decreasing concentration of Mn^{2+} ions in solution (relative to the rate of decrease of Ni^{2+}), more Ni^{2+} ions from $[Ni(NH_3)n]^{2+}$ complexes become available and eventually precipitate, disproportionately to the target composition, on the surface of the particles.

However, in the overall process leading to the Ni enrichment at the surface of the particles, there are two confounding factors which could be contributing: the tendency for Ni to form a stable ammonia complex $[Ni(NH_3)n]^{2+}$ as just discussed, and the higher K_{sp} value of $NiCO_3$ compared to $MnCO_3$. Interestingly, when using sodium bicarbonate in to synthesize $Ni_{0.35}Mn_{0.65}CO_3$, where there was no ammonia complex formation, and the targeted Ni content could be achieved a core-shell-like structure with surface enrichment of Ni on the secondary particles was still observed (see Figure S1 b). The surface exhibited an increased concentration of Ni, twice the amount compared to the core region. This suggests that the difference in K_{sp} values for $NiCO_3$ and $MnCO_3$ drives the initial nucleation process resulting in a Mn-rich core and the enrichment of Ni on the surface, while the final overall Ni content of particles is strongly dependent, in this case, by use of NH_4HCO_3 vs. $NaHCO_3$ in the initial reaction solutions.

3.5 Electrochemical testing

The detailed studies herein show that controlling the small-scale, batch mode synthesis of Mn-rich carbonates can be difficult. However, the $Ni_{0.35}Mn_{0.65}CO_3$, synthesized without ammonia (section 3.4 and sample in Figure S1), resulted in the desired composition with ICP analysis giving $Ni_{0.34}Mn_{0.66}$, and microscopy studies showing relatively homogeneous distribution of Mn and Ni in the precursor product. To test this sample as a precursor for the synthesis of a lithium-ion battery cathode, calcination/lithiation was carried out at 850°C in air to achieve a final composition of $Li_{1.13}Ni_{0.30}Mn_{0.57}O_2$. Powder XRD data (Figure S5) showed the expected pattern of a well-layered LMR-NM material and SEM (Figure S6) revealed a uniform, spherical morphology for the final product. As a first test to evaluate whether the electrochemical properties are also as expected, cathode-electrodes were fabricated from the cathode powder and tested in coin-cells. Figure 9 reveals (a) the rate capability and (b) the cycling performance of the cells against Li metal anodes.

The cells underwent a first-cycle activation between 4.7-2.0 V and were subsequently cycled between 4.5-2.5 V. The electrode provided a capacity of ~170 mAh/g at a 2C discharge rate (400 mA/g). Furthermore, a capacity of ~200 mAh/g at C/10, with excellent stability, was delivered over the 50 cycles on test. Figure 9(c) shows the voltage profiles of the 1st and 2nd cycles confirming the expected, characteristic behavior of the LMR-NM composite structure and confirming the validity of the synthesis. A more detailed electrochemical evaluation, using graphite full-cells, will be carried out in future studies to assess other characteristics such as cycle-life and impedance behavior.

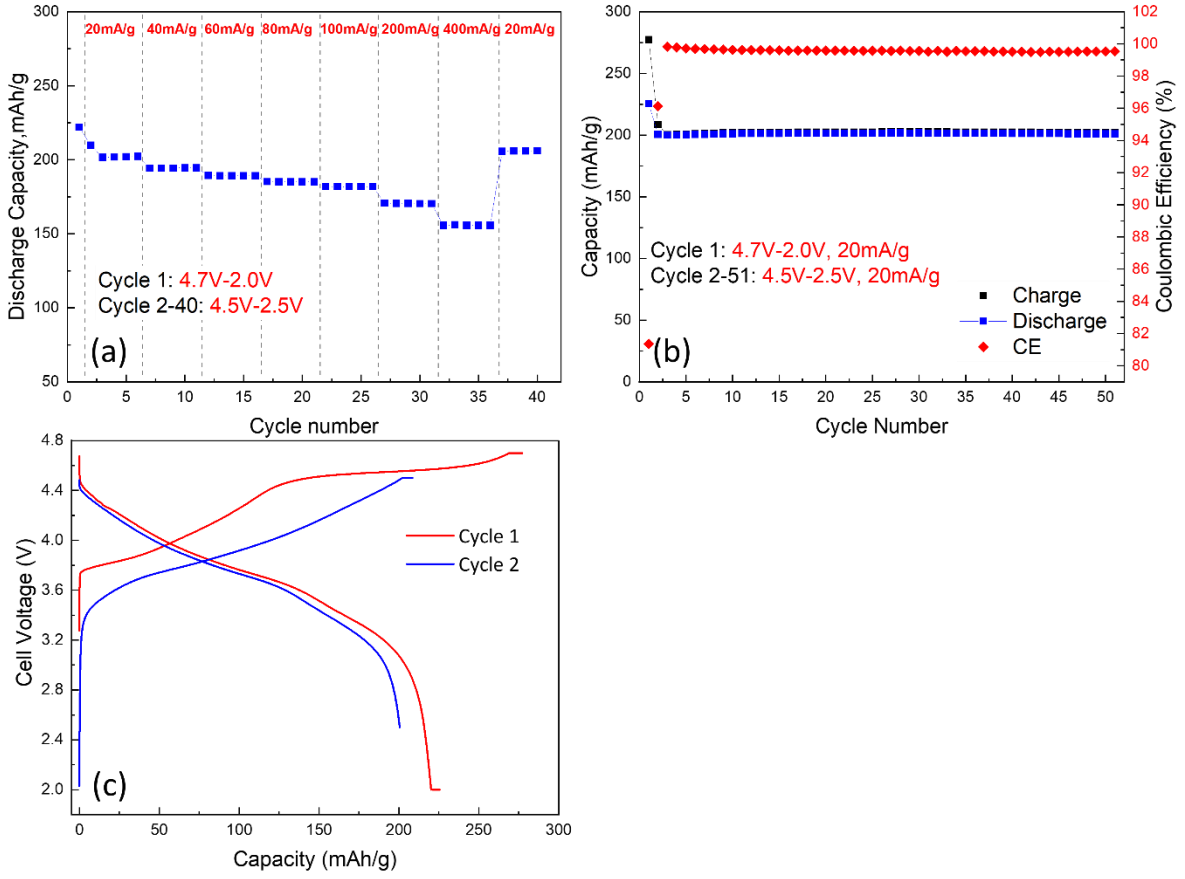

Figure 9 Electrochemical performance for the lithiated x=0.35 precursor ($Li_{1.13}Ni_{0.30}Mn_{0.57}O_2$). (a) Rate capability between 4.5-2.5 V vs. Li/Li^+ at different discharge currents (mA/g) as listed along the top of the graph, charging current was kept constant for all cycles at 20mA/g (b) Cycling data between 4.5-2.5 V vs. Li/Li^+ at C/10 (20mA/g) at 30°C. (c) Voltage profiles of the 1st (4.7-2.0 V) and 2nd (4.5-2.5 V) cycles.

4. Conclusions

In this study, $Ni_xMn_{1-x}CO_3$ have been synthesized via batch mode co-precipitation in order to gain insights into the synthesis and control of earth-abundant, Mn-rich, Co-free precursors for cathode-oxides. A series of samples are generated by varying x in $Ni_xMn_{1-x}CO_3$ (x=0, 0.1, 0.3, 0.5, 0.7, 0.9), and each of them was studied experimentally and/or computationally in terms of final composition, crystallinity, transition metal distribution, and particle morphology to decipher the impact of Ni amount in reaction solutions.

Although all samples formed the expected R-3c, calcite structure typical of carbonate precursors, significant differences were observed in particle size and crystallinity as a function of x. In particular, a transition from uniform morphologies (e.g., spherical, monodisperse, pseudo single crystalline particles) to bimodal, polycrystalline particles was observed for Ni concentrations above x= ~0.5.

In addition, the final Ni concentration was significantly lower than the targeted value for all but the highest Ni concentration (x=0.9). Computational modeling was used to attribute this effect to the high K_{sp} of $NiCO_3$ relative to $MnCO_3$ and the strong tendency of Ni^{2+} to react with NH_4^+ in solution to form $[Ni(NH_3)n]^{2+}$. Likewise, the high supersaturation ratio of $MnCO_3$, especially in Mn-rich compositions, drives initial nucleation and the enrichment of Mn within the core of the particles. This effect, coupled to formation of $[Ni(NH_3)n]^{2+}$when using NH_4HCO_3, leads to Ni enrichment at particle surfaces. Using $NaHCO_3$ to avoid the formation of $[Ni(NH_3)n]^{2+}$allows for the targeted Ni content to be achieved but Ni is still disproportionately found on the surface due to the fast nucleation of $MnCO_3$ (low K_{sp}/high SSR) in the initial stages of the reaction. Subsequent

calcination/lithiation of this precursor showed the expected structure and electrochemical behavior typical of LMR electrodes.

These results provide insights into the reaction conditions that control the properties of Mn-rich precursors for the synthesis of cathode-oxides and give insights into better synthetic control towards practical application of this class of materials.

Acknowledgements

Support from the Vehicle Technologies Office of the U.S. Department of Energy, particularly from the *Earth-abundant Cathode Active Materials (EaCAM)* consortium under Tien Duong, Carine Steinway, and Brian Cunningham, is gratefully acknowledged. Work performed at the Center for Nanoscale Materials, a U.S. Department of Energy Office of Science User Facility, was supported by the U.S. DOE, Office of Basic Energy Sciences, under Contract No. DE-AC02-06CH11357. The authors also thank Gerald T. Jeka and Ozge Kahvecioglu of the Materials Engineering Research Facility (MERF) at ANL for ICP analysis.

Supporting Information

SEM-EDS mapping $Ni_xMn_{1-x}CO_3$ (x=0.35; x=0.7); plot of supersaturation ratio of $MnCO_3$ and $NiCO_3$; equations, and table of parameters for computational calculations and simulation of distribution of the primary particles of $Ni_xMn_{1-x}CO_3$ (x=0.3; x=0.5) within secondary particles; XRD powder diffraction pattern and SEM of the LMR-NM cathode tested in Figure 9 of the main text. (PDF)

References

(1) Thackeray, M. M.; Wolverton, C.; Isaacs, E. D. Electrical energy storage for transportation—approaching the limits of, and going beyond, lithium-ion batteries. *Energy & Environmental Science* **2012**, *5* (7), 7854-7863.
(2) Nitta, N.; Wu, F.; Lee, J. T.; Yushin, G. Li-ion battery materials: present and future. *Materials today* **2015**, *18* (5), 252-264.
(3) Julien, C.; Mauger, A.; Zaghib, K.; Groult, H. Optimization of layered cathode materials for lithium-ion batteries. *Materials* **2016**, *9* (7), 595.
(4) Gutierrez, A.; Kirner, J. T.; Saray, M. T.; Avdeev, M.; Geng, L.; Yassar, R. S.; Lu, W.; Croy, J. Critical Barriers to Successful Implementation of Earth-Abundant, Mn-Rich Cathodes for Vehicle Applications and Beyond: The Effect of Particle Morphology. *Journal of The Electrochemical Society* **2022**, *169* (2), 020574. DOI: 10.1149/1945-7111/ac5545.
(5) Croy, J. Earth-abundant Cathode Active Materials for Li-Ion Batteries: Program Overview. In *Annual Merit Review*, Washington, D.C.; June 12-15, **2023**, BAT569.
(6) Gutierrez, A.; Tewari, D.; Chen, J.; Srinivasan, V.; Balasubramanian, M.; Croy, J. R. Earth-Abundant, Mn-Rich Cathodes for Vehicle Applications and Beyond: Overview of Critical Barriers. *Journal of The Electrochemical Society* **2023**, *170*, 030509.
(7) Dong, H.; Koenig, G. M. A review on synthesis and engineering of crystal precursors produced via coprecipitation for multicomponent lithium-ion battery cathode materials. *CrystEngComm* **2020**, *22* (9), 1514-1530.
(8) Caurant, D.; Baffier, N.; Garcia, B.; Pereira-Ramos, J. Synthesis by a soft chemistry route and characterization of LiNixCo1− xO2 (0≤ x≤ 1) cathode materials. *Solid State Ionics* **1996**, *91* (1-2), 45-54.
(9) Lu, Z.; MacNeil, D.; Dahn, J. Layered cathode materials Li [Ni x Li (1/3− 2x/3) Mn (2/3− x/3)] O 2 for lithium-ion batteries. *Electrochemical and Solid-State Letters* **2001**, *4* (11), A191.
(10) Van Bommel, A.; Dahn, J. Analysis of the growth mechanism of coprecipitated spherical and dense nickel, manganese, and cobalt-containing hydroxides in the presence of aqueous ammonia. *Chemistry of Materials* **2009**, *21* (8), 1500-1503.
(11) Lee, Y.; Sun, Y.; Ota, S.; Miyashita, T.; Yoshio, M. Preparation and characterization of nano-crystalline LiNi0. 5Mn1. 5O4 for 5 V cathode material by composite carbonate process. *Electrochemistry Communications* **2002**, *4* (12), 989-994.
(12) Deng, C.; Liu, L.; Zhou, W.; Sun, K.; Sun, D. Effect of synthesis condition on the structure and electrochemical properties of Li [Ni1/3Mn1/3Co1/3] O2 prepared by hydroxide co-precipitation method. *Electrochimica acta* **2008**, *53* (5), 2441-2447.
(13) Chen, W.-C.; Song, Y.-F.; Wang, C.-C.; Liu, Y.; Morris, D. T.; Pianetta, P. A.; Andrews, J. C.; Wu, H.-C.; Wu, N.-L. Study on the synthesis–microstructure-performance relationship of layered Li-excess nickel–manganese oxide as a Li-ion battery cathode prepared by high-temperature calcination. *Journal of Materials Chemistry A* **2013**, *1* (36), 10847-10856.
(14) Lee, M.-H.; Kang, Y.-J.; Myung, S.-T.; Sun, Y.-K. Synthetic optimization of Li [Ni1/3Co1/3Mn1/3] O2 via co-precipitation. *Electrochimica Acta* **2004**, *50* (4), 939-948.

(15) Wang, D.; Belharouak, I.; Koenig, G. M.; Zhou, G.; Amine, K. Growth mechanism of Ni0. 3Mn0. 7CO3 precursor for high capacity Li-ion battery cathodes. *Journal of Materials Chemistry* **2011**, *21* (25), 9290-9295.
(16) Garcia, J. C.; Barai, P.; Chen, J.; Gutierrez, A.; Wen, J.; Arslan, I.; Wang, X.; Fister, T. T.; Iddir, H.; Srinivasan, V. Predicting Morphological Evolution during Coprecipitation of MnCO3 Battery Cathode Precursors Using Multiscale Simulations Aided by Targeted Synthesis. *Chemistry of Materials* **2020**, *32* (21), 9126-9139.
(17) Huang, Z.; Wang, X.; Feng, W.; Li, W.; Shi, Z.; Lei, Z. Effect of sintering temperature on the electrochemical performance of Li-rich Mn-basfed cathode material Li1. 2Mn0. 54Ni0. 13Co0. 13O2 by co-precipitation method. *Journal of Electroanalytical Chemistry* **2021**, *895*, 115439.
(18) Huang, Z.; Feng, W.; Lei, Z.; Li, W.; Zhao, W. Effect of ZIF-67 derivative Co3O4 on Li-rich Mn-based cathode material Li1. 2Mn0. 54Ni0. 13Co0. 13O2. *Ceramics International* **2021**, *47* (24), 34492-34500.
(19) Cho, T.; Park, S.; Yoshio, M.; Hirai, T.; Hideshima, Y. Effect of synthesis condition on the structural and electrochemical properties of Li [Ni1/3Mn1/3Co1/3] O2 prepared by carbonate co-precipitation method. *Journal of power sources* **2005**, *142* (1-2), 306-312.
(20) Robinson, J. P.; Koenig Jr, G. M. Tuning solution chemistry for morphology control of lithium-ion battery precursor particles. *Powder Technology* **2015**, *284*, 225-230.
(21) Qiu, L.; Zhang, M.; Song, Y.; Wu, Z.; Hu, K.; Yue, L.; Zhang, J.; Ming, Y.; Xiang, W.; Wang, G.; Liu, Y.; Sun, Y.; Guo, X. The structure-activity relationship between precursor fine structure and cathode performance in ultra-high Ni layered oxide. *Chemical Engineering Science* **2022**, *260*, 117865.
(22) Jiang, Y.; Guo, F.; Qiu, L.; Liu, T.; Hu, Y.; Yang, W.; Liu, Y.; Sun, Y.; Wu, Z.; Song, Y.; Guo, X. Enhancing the Integral Structural and Thermal Stability of Ultrahigh-Ni Cathodes via Morphology Refinement and In Situ Interfacial Engineering. *ACS Applied Materials & Interfaces* **2023**, *15* (29), 35072-35081.
(23) Guo, F.; Hu, Y.; Qiu, L.; Jiang, Y.; Deng, Y.; Zhou, J.; Zheng, Z.; Liu, Y.; Sun, Y.; Wu, Z.; Song, Y.; Guo, X. Surface energy alteration-derived grain size regulation countering capacity deterioration in high-voltage single-crystal Ni-rich cathodes. *Journal of Materials Chemistry A* **2023**, *11* (22), 11819-11830.
(24) Fan, X. M.; Huang, Y. D.; Wei, H. X.; Tang, L. B.; He, Z. J.; Yan, C.; Mao, J.; Dai, K. H.; Zheng, J. C. Surface modification engineering enabling 4.6 V single-crystalline Ni-rich cathode with superior long-term cyclability. *Advanced Functional Materials* **2022**, *32* (6), 2109421.
(25) Zheng, J.; Yan, P.; Estevez, L.; Wang, C.; Zhang, J.-G. Effect of calcination temperature on the electrochemical properties of nickel-rich LiNi0. 76Mn0. 14Co0. 10O2 cathodes for lithium-ion batteries. *Nano Energy* **2018**, *49*, 538-548.
(26) Barai, P.; Feng, Z.; Kondo, H.; Srinivasan, V. Multiscale computational model for particle size evolution during coprecipitation of Li-ion battery cathode precursors. *The Journal of Physical Chemistry B* **2019**, *123* (15), 3291-3303.
(27) Stadelmann, P. *JEMS*. https://www.jems-swiss.ch/ (accessed 2023 July 31).
(28) Xi, X.; Abe, H.; Kuruma, K.; Harada, R.; Shui, A.; Naito, M. Novel Co-precipitation method to synthesize NiO–YSZ nanocomposite powder for solid oxide fuel cell. *Advanced Powder Technology* **2014**, *25* (2), 490-494.

(29) Vaccari, M.; Barontini, F.; Bertei, A.; Puccini, M.; Tognotti, L. Co-precipitation of Cathode Active Materials Precursors in Lithium-ion Batteries Recycling: Experiments and Modeling. *Chemical Engineering Transactions* **2023**, *99*, 169-174.
(30) Grgicak, C. M.; Green, R. G.; Du, W. F.; Giorgi, J. B. Synthesis and characterization of NiO–YSZ anode materials: precipitation, calcination, and the effects on sintering. *Journal of the American Ceramic Society* **2005**, *88* (11), 3081-3087.

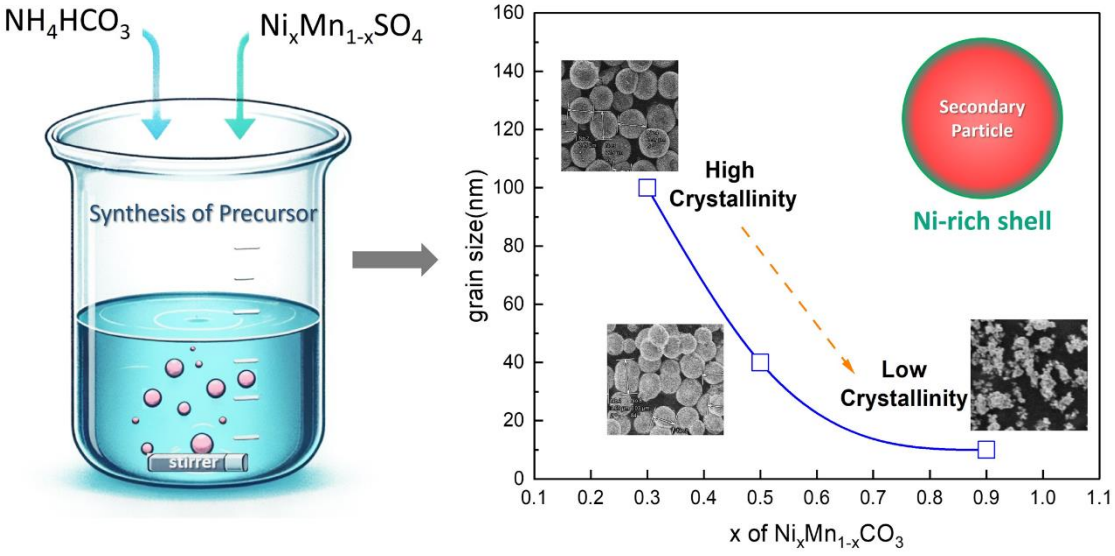
NH4HCO3
NixMn1-xSO4
Synthesis of Precursor
surrer
grain size(nm)
x of NixMn1-xCO3
High Crystallinity
Low Crystallinity
Secondary Particle
Ni-rich shell